Nano Research

Open Access

Research Article

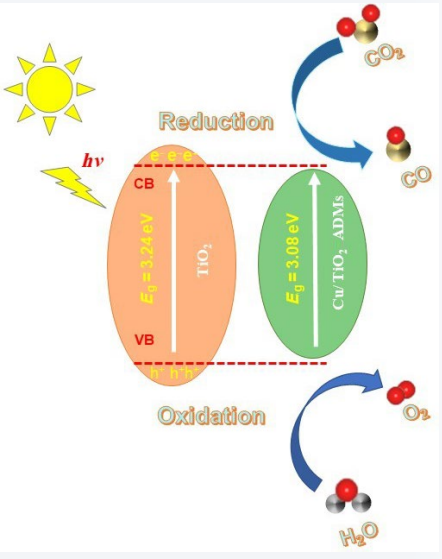
Engineering of atomically dispersed Cu on TiO_2 via flash Joule heating for solar-driven CO_2 reduction

Khadija Tul Kubra[1,§], Jian Lei[2,§], Zhongliao Wang[3,§], Shuaikang Sang[1], You Li[1], Saira Man[1], Zakaria Ismail[1], Chao Zhang[2] ✉, Jingxiang Low[4], Ran Long[1], and Yujie Xiong[1,2] ✉

[1] *School of Chemistry and Materials Science and National Synchrotron Radiation Laboratory, University of Science and Technology of China, Hefei 230026, China*
[2] *Anhui Engineering Research Centre of Carbon Neutrality, The Key Laboratory of Functional Molecular Solids, Ministry of Education, Anhui Laboratory of Molecular-Based Materials, College of Chemistry and Materials Science, Anhui Normal University, Wuhu 241002, China*
[3] *Key Laboratory of Green and Precise Synthetic Chemistry and Applications, Ministry of Education, Huaibei Normal University, Huaibei 235000, China*
[4] *School of Physical Science and Engineering, Tiangong University, Tianjin 300378, China*
[§] *Khadija Tul Kubra, Jian Lei, and Zhongliao Wang contributed equally to this work.*

Cite this article: *Nano Research*, **2026**, *19*, 94908854. https://doi.org/10.26599/NR.2026.94908854

ABSTRACT: Constructing photocatalysts decorated with atomically dispersed metal species (ADMs) represents a pivotal strategy to maximize atom utilization and tailor active sites for efficient carbon dioxide (CO_2) reduction. However, conventional synthesis strategies, typically relying on tedious wet-chemistry or prolonged thermal calcination, often suffer from slow kinetics that inevitably drive the thermodynamic aggregation of metastable single atoms or nanoclusters into less active nanoparticles. Herein, we bypassed these limitations by developing a facile flash Joule heating (FJH) strategy to engineer stable Cu ADMs on TiO_2 via an ultrafast and millisecond-scale heating-quenching process. This non-equilibrium thermal shock effectively stabilizes the metal species before thermal diffusion can occur, ensuring a robust metal–support interaction, as unambiguously confirmed by aberration-corrected high-angle annular dark-field scanning transmission electron microscopy (HAADF-STEM) and X-ray absorption fine structure (XAFS) analyses. Consequently, the optimized $Cu_{1.0}/TiO_2$ delivers an approximately 10-fold enhancement in CO evolution compared to pristine TiO_2 under simulated solar irradiation. Comprehensive *in-situ* diffuse reflectance Fourier transform spectroscopy (DRIFTS) and photoelectrochemical measurements reveal that these isolated Cu sites function as superior electron-trapping centers, which significantly accelerate interfacial charge transfer kinetics and promote the activation of critical reaction intermediates. This work establishes FJH as a versatile and scalable platform for overcoming the stability-dispersion trade-off in the rational design of high-performance photocatalysts.



KEYWORDS: Cu_x/TiO_2 atomically dispersed metal species (ADMs), flash Joule heating (FJH), $Cu_{1.0}/TiO_2$, photocatalytic CO_2 reduction

1 Introduction

The growing consumption of fossil fuels has driven atmospheric carbon dioxide (CO_2) concentrations to critical levels, necessitating the development of sustainable technologies to close the anthropogenic carbon cycle. Artificial photosynthesis, which utilizes semiconductor materials to harvest solar energy for the reduction of CO_2 into value-added chemicals, offers a promising green pathway to simultaneously alleviate energy shortages and environmental crises [1–4]. An ideal photocatalyst requires a synergistic combination of broad light absorption, efficient charge separation, and abundant surface active sites. However, most single-component

Received: April 21, 2026; **Revised:** May 16, 2026
Accepted: May 19, 2026

✉Address correspondence to Chao Zhang, zc1992@ustc.edu.cn; Yujie Xiong, yjxiong@ustc.edu.cn

semiconductors intrinsically suffer from sluggish charge transfer kinetics and rapid electron–hole recombination, creating a fundamental bottleneck that necessitates surface engineering with co-catalysts to unlock their full catalytic potential [5–7].

Decorating semiconductors with metal species is a proven strategy to modulate surface electronic states and accelerate reaction kinetics. While decorating with noble metals has traditionally dominated this field, the high cost and scarcity have catalyzed a shift toward earth-abundant alternatives, particularly transition metals, such as copper (Cu) [8–11]. To maximize the atomic utilization efficiency of these non-noble metals, the field is rapidly evolving from nanoscale particles toward the ultimate limit of atomically dispersed metal species (ADMs). These isolated sites not only minimize material usage but also offer unique coordination environments that can dramatically enhance selectivity [12–15]. Nevertheless, the practical realization of such high-density ADMs is severely hindered by the stability–dispersion trade-off, as the high surface free energy of isolated metal species inevitably drives them to aggregate into thermodynamically stable clusters during the prolonged high-temperature treatments inherent to conventional synthesis [16–20].

Overcoming this thermodynamic barrier requires a paradigm shift from equilibrium-based synthesis to non-equilibrium kinetic control. Flash Joule heating (FJH), an emerging electro-thermal technique, provides a powerful solution by generating ultrahigh temperatures (> 1500 °C) within milliseconds, followed by rapid quenching rates exceeding 10^4 K·s^{-1}. This heat shock mechanism effectively decomposes precursors while kinetically stabilizing the metal species in their dispersed state before thermal diffusion and agglomeration can occur [21–24]. Unlike traditional wet-chemistry or calcination methods that are often time-consuming and energy-intensive, FJH offers several advantages, including ultrafast processing, operational simplicity, solvent-free synthesis, high energy efficiency, and scalability. These features make FJH a promising strategy for the large-scale synthesis of advanced atomically dispersed catalytic materials. While FJH has demonstrated remarkable success in carbon material processing, its potential as a universal platform for constructing robust atomically dispersed metal–oxide interfaces toward solar-to-fuel conversion remains largely underexplored and merits systematic investigation [25–29].

Herein, employing TiO_2 as a model semiconductor support, we demonstrated a facile FJH strategy to achieve the controlled synthesis of atomically dispersed Cu species via this ultrafast heating-cooling process. By systematically regulating the pulse parameters, we successfully anchored isolated Cu species with a well-defined local coordination environment, as unambiguously confirmed by aberration-corrected high-angle annular dark-field scanning transmission electron microscopy (HAADF-STEM) and X-ray absorption fine structure (XAFS) analyses. The resulting $Cu_{1.0}/TiO_2$ catalyst exhibits an approximately 10-fold enhancement in photocatalytic CO evolution under simulated solar irradiation, attributed to the formation of efficient electron-trapping centers that boost interfacial charge separation. This work not only provides fundamental insights into the structure–activity relationship of FJH-derived catalysts but also establishes a universal and scalable methodology for designing high-performance ADMs for diverse energy conversion applications.

2 Results and discussion

2.1 Formation and structural characterization of Cu_x/TiO_2 ADMs

In this work, the carbon-supported Cu_x/TiO_2 ADMs (x = 0.5, 1, 2, and 3 corresponding to wt.% Cu), where were synthesized via a FJH strategy (Fig. S1 in the Electronic Supplementary Material (ESM)), where the precursor-loaded substrate undergoes an ultrafast thermal shock (ca. 1000 °C within ms). This non-equilibrium process utilizes rapid Joule heating to decompose metal precursors, followed immediately by an ultrafast quenching rate that kinetically stabilizes the Cu species before diffusion can occur. Consequently, the thermodynamically driven aggregation of atomically dispersed Cu species is effectively suppressed, securing the stabilization of isolated Cu sites on the TiO_2 support [30–32]. To verify the successful synthesis of carbon-supported Cu_x/TiO_2 ADMs, the morphology and atomic structure were comprehensively analyzed. Field emission scanning electron microscopy (FESEM) (Figs. S2(a)–S2(e) in the ESM) and transmission electron microscopy (TEM) images (Fig. 1(a) and Figs. S2(a')–S2(e') in the ESM) reveal that the $Cu_{1.0}/TiO_2$ ADMs retain the particulate morphology of the TiO_2 support. Despite the thermal shock, the TiO_2 nanoparticles maintain a uniform size distribution without severe sintering, highlighting the structural preservation capability of the FJH method. High-resolution TEM (HRTEM) further elucidates the crystallinity of the support (Fig. 1(b)). Specifically, clear lattice fringes with a d-spacing of 0.35 nm can be observed, corresponding to the (101) plane of anatase TiO_2.

To provide direct visual evidence of the atomic dispersion of Cu, aberration-corrected HAADF-STEM was employed. As shown in Figs. 1(c) and 1(d), and Fig. S3 in the ESM, the TiO_2 support exhibits a highly crystalline structure with lattice fringes of 0.24 nm, assigned to the (004) plane. In addition, owing to the Z-contrast mechanism, where intensity is proportional to Z^2, the heavier Cu atoms (Z = 29) appear as distinct and bright regions dispersed against the lighter Ti (Z = 22) background. These bright features are isolated and uniformly distributed without forming larger clusters, unambiguously confirming the formation of ADMs [33]. This atomic-level dispersion is further corroborated by STEM-energy dispersive X-ray spectroscopy (EDS) elemental mapping (Figs. 1(e)–1(h) and Fig. S4 in the ESM), which demonstrates a homogeneous overlap of Cu, Ti, and O signals throughout the nanoparticle architecture, ruling out significant phase segregation (Table S1 in the ESM). The actual content of the copper on the $Cu_{1.0}/Ti$ is determined to be ca. 0.8%, using inductively coupled plasma-optical emission spectroscopy (ICP-OES) (Table S2 in the ESM).

The crystalline phase and chemical state of the catalysts were further investigated. The X-ray diffraction (XRD) patterns for all Cu_x/TiO_2 samples are identical to TiO_2 (Fig. 1(i) and Fig. S5 in the ESM), indexing to the anatase phase (JCPDS No. 21-1272). The absence of characteristic copper oxide peaks, even at relatively high loadings, supports the STEM findings that Cu species are highly dispersed, below the detection limit of XRD. Raman spectroscopy (Fig. 1(j)) reinforces this finding, where all samples exhibit the Raman peaks attributed to the anatase TiO_2 (E_g at ca. 149 cm^{-1}, B_{1g} at ca. 400 cm^{-1}, and A_{1g} at ca. 641 cm^{-1}). The lack of peak shifting or broadening upon Cu introduction suggests that the

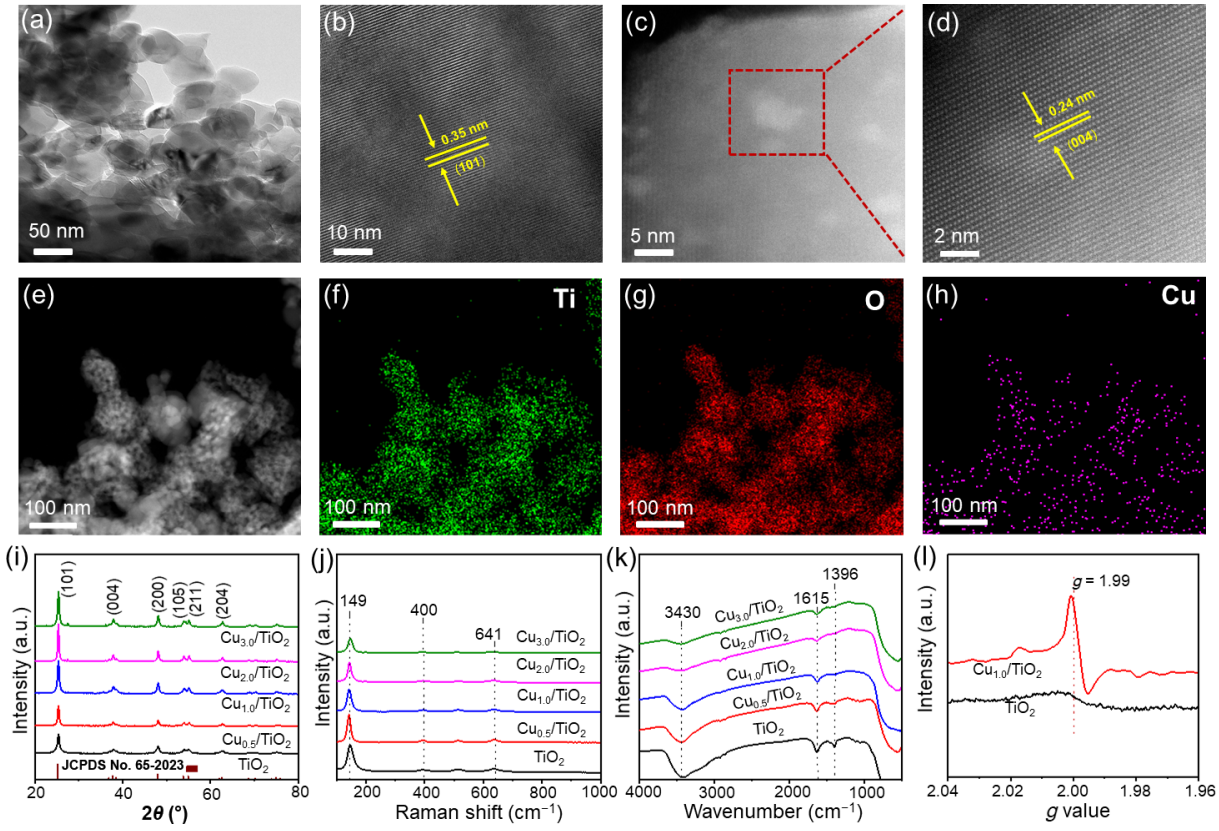


Figure 1 Characterization of TiO_2 and Cu_x/TiO_2 ADMs. (a) TEM image of $Cu_{1.0}/TiO_2$ ADMs. (b) HRTEM image of $Cu_{1.0}/TiO_2$ ADMs. (c) HAADF-STEM raw image of $Cu_{1.0}/TiO_2$ ADMs. (d) Magnified HAADF-STEM image of $Cu_{1.0}/TiO_2$ ADMs. ((e)–(h)) Elemental mappings of $Cu_{1.0}/TiO_2$ ADMs. ((i)–(l)) XRD, Raman, FTIR, and EPR results of TiO_2 and Cu_x/TiO_2 ADMs, respectively.

bulk lattice structure of TiO_2 remains intact and Cu species are primarily anchored at the surface or subsurface defects rather than altering the bulk crystal symmetry [34, 35].

To probe the local coordination environment and defect sites, Fourier transform infrared (FTIR) and electron paramagnetic resonance (EPR) spectroscopies were utilized. FTIR spectra (Fig. 1(k)) display characteristic bands for adsorbed water (ca. 3430 cm^{-1}) and surface hydroxyl groups (ca. 1615 and 1396 cm^{-1}). The preservation of these surface hydroxyls is vital, as they often serve as adsorption sites for CO_2 reactants [36]. Furthermore, EPR provides compelling evidence for the electronic state of the copper species (Fig. 1(l)). While pristine TiO_2 is EPR silent in this region, the $Cu_{1.0}/TiO_2$ exhibit a distinct and strong paramagnetic signal centered at a g value of ca. 2.00. This signal is characteristic of isolated Cu^{2+} species with unpaired electrons, which can be coordinated in a distorted geometry on the TiO_2 surface. The presence of this signal confirms that the Cu species are not metallic Cu^0, which is diamagnetic and EPR silent, but are electronically coupled to the support, creating active sites favorable for charge separation and photocatalytic redox reactions.

The optical properties of pristine TiO_2 and Cu_x/TiO_2 were investigated using ultraviolet–visible diffuse reflectance spectroscopy (UV–Vis DRS), and the results are shown in Fig. 2(a). Pristine TiO_2 exhibits strong intrinsic absorption solely in the ultraviolet region with an absorption edge at ca. 380 nm. In distinct contrast, all Cu-modified samples display a bathochromic shift and enhanced light absorption extending into the visible range of 400–700 nm. With increasing Cu loading, the absorption intensity progressively rises, suggesting that the incorporation of Cu species introduces new energy levels within the bandgap, due to d–d internal transitions of Cu^{2+} or charge transfer transitions between Cu ions and the TiO_2. Based on the UV–Vis DRS spectra, Tauc plots were generated to determine the optical bandgaps (Fig. 2(b)). The intrinsic bandgap (E_g) of pristine TiO_2 is calculated to be ca. 3.24 eV. Upon Cu incorporation, the bandgap narrows, reaching 3.08 eV for $Cu_{1.0}/TiO_2$ and decreasing further to 2.80 eV for $Cu_{3.0}/TiO_2$. This narrowing is attributed to the hybridization of Cu 3d orbitals with O 2p orbitals, which creates impurity energy levels and effectively reduces the energy required for electron excitation [10, 34, 37]. To elucidate the band edge alignment, valence band X-ray photoelectron spectroscopy (VB-XPS) was employed (Fig. 2(c)). The valence band maximum (VBM) of pristine TiO_2 is located at ca. 2.50 eV, whereas the VBM of $Cu_{1.0}/TiO_2$ shifts upward to ca. 2.10 eV. These mid-gap electronic transitions leading to enhanced light absorption range into the longer wavelength region, thereby promoting solar light harnessing capacity. To further understand the electronic structure evolution upon Cu anchoring, density of states (DOS) calculations were carried out (Figs. 2(d) and 2(e)). By combining the E_g from the Tauc plots with the VBM positions, the conduction band minimum (CBM) potentials were calculated using the equation $E_g = E_{VB} - E_{CB}$ (Fig. 2(f)). Consequently, the CBM of pristine TiO_2 is determined to be −0.74 eV vs. normal hydrogen electrode (NHE), pH = 7, while the $Cu_{1.0}/TiO_2$ exhibits a significantly more negative CBM at −0.98 eV. This upward shift in the conduction band position is critical for photocatalysis. A CBM of −0.98 eV provides a stronger thermodynamic driving force (overpotential) for the reduction of CO_2 compared to pristine TiO_2. Therefore, the optimized band structure of $Cu_{1.0}/TiO_2$ not only

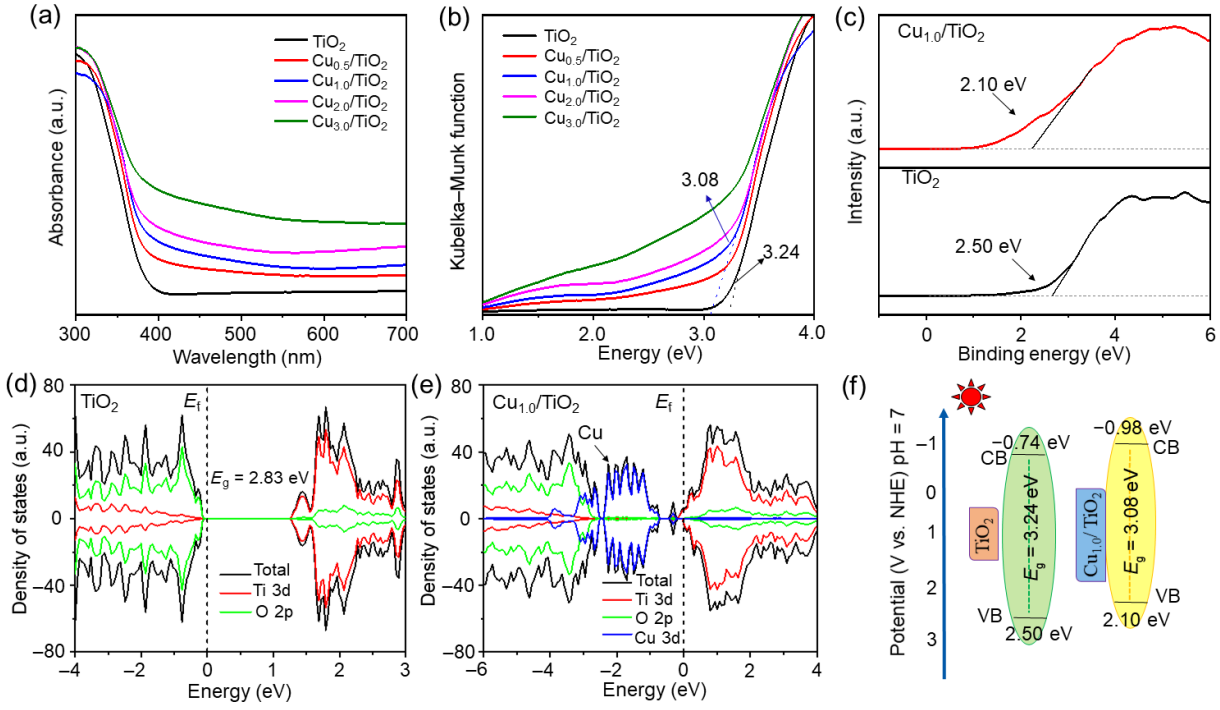


Figure 2 (a) UV–Vis DRS spectra of the TiO_2 and Cu_x/TiO_2. (b) Bandgaps for TiO_2 and Cu_x/TiO_2. (c) Valence band XPS spectra for TiO_2 and $Cu_{1.0}/TiO_2$. ((d) and (e)) Density of state spectra of (d) TiO_2 and (e) $Cu_{1.0}/TiO_2$. (f) Schematic energy level diagram of TiO_2 and $Cu_{1.0}/TiO_2$.

broadens visible light utilization but also energetically favors the electron transfer required for efficient CO_2 reduction [36, 38]. The consistent trends observed in both experimental characterization and theoretical calculations corroborate the formation of Cu-induced mid gap electronic states, which shift the electronic structure closer to the fermi level. These defect-related states facilitate more efficient charge separation under visible light irradiation.

X-ray absorption fine structure (XAFS) spectroscopy was utilized to rigorously probe the electronic structure and local coordination environment of the Cu species. The Cu K-edge X-ray absorption near-edge structure (XANES) spectra reveal that the absorption edge position of the $Cu_{1.0}/TiO_2$ is situated significantly higher than that of Cu foil and aligns closely with the CuO reference (Fig. 3(a)). This positive energy shift indicates that the anchored Cu species exist in an oxidized state ($Cu^{\delta+}$), rather than a metallic state (Cu^0). To decipher the atomic-level dispersion, Fourier-transformed extended X-ray absorption fine structure (FT-EXAFS) analysis was performed (Fig. 3(b)) [19, 39–41]. The spectrum of $Cu_{1.0}/TiO_2$ exhibits a dominant main peak at ca. 1.5 Å, corresponding to the first coordination shell of Cu–O scattering. In addition, no characteristic peaks for Cu–Cu (metallic Cu) or Cu–O–Cu (bulk copper oxides) scattering are observed in the higher distance range (2–3 Å). This absence provides robust evidence that the Cu atoms are isolated on the support without aggregation. Quantitative EXAFS fitting further reveals a coordination number (CN) of approximately 2.60 for the Cu–O shell with a bond length of 1.90 Å (Table S3 in the ESM). This CN is markedly lower than that of bulk CuO (CN = 4), suggesting that the Cu ADMs possess a coordinatively unsaturated environment, which is highly favorable for the adsorption and activation of CO_2 molecules [42].

To further elucidate the surface chemical composition and the strong metal–support interactions (SMSI), XPS was employed (Figs. 3(c)–3(f) and Table S4 in the ESM). The survey spectrum confirms the coexistence of Ti, O, C, and Cu elements (Fig. 3(c)). In the high-resolution O 1s spectra (Fig. 3(d)), the peaks at 529.95, 530.82, and 532.35 eV are assigned to lattice oxygen (O^{2-}), surface hydroxyls (OH^-), and adsorbed oxygen species (O_{ads}), respectively. Notably, compared to pristine TiO_2, the $Cu_{1.0}/TiO_2$ exhibits a higher ratio of surface hydroxyl/adsorbed oxygen species and a positive shift in binding energy is mainly attributed to the strong electronic interaction and charge transfer between the atomically dispersed Cu species and the TiO_2 support, which alters the local electronic environment of Ti and O atoms [41, 42]. This suggests that the introduction of Cu induces the formation of surface oxygen vacancies and modifies the surface electron density, facilitating reactant adsorption. Evidence of electronic coupling is further highlighted in the Ti 2p spectra (Fig. 3(e)). The Ti $2p_{3/2}$ and $2p_{1/2}$ peaks for $Cu_{1.0}/TiO_2$ shift to higher binding energies (458.79 and 464.45 eV) relative to pristine TiO_2 (458.60 and 464.30 eV). This positive shift indicates a decrease in electron density on the Ti sites, implying an electron transfer from the TiO_2 toward the anchored Cu species due to the strong interfacial electronic interaction. Finally, the Cu 2p high-resolution spectrum displays a main peak at 933.28 eV (Fig. 3(f)), accompanied by distinct shake-up satellite peaks (ca. 940–945 eV). These satellite features are the fingerprint of paramagnetic Cu^{2+} (d^9) species, ruling out the presence of Cu^+ (d^{10}) or metallic Cu which does not exhibit such satellites. This confirms that the atomically dispersed Cu sites are stabilized in a positive oxidation state (predominantly Cu^{2+}) on the TiO_2 [43]. Collectively, the XAFS and XPS results confirm that the FJH strategy successfully constructs isolated and positively charged Cu sites that interact strongly with the support, creating efficient centers for charge trapping and catalytic turnover.

2.2 Photocatalytic CO_2 reduction performance

After establishing the structural integrity, surface chemistry, and optical response of the Cu_x/TiO_2, their photocatalytic performance

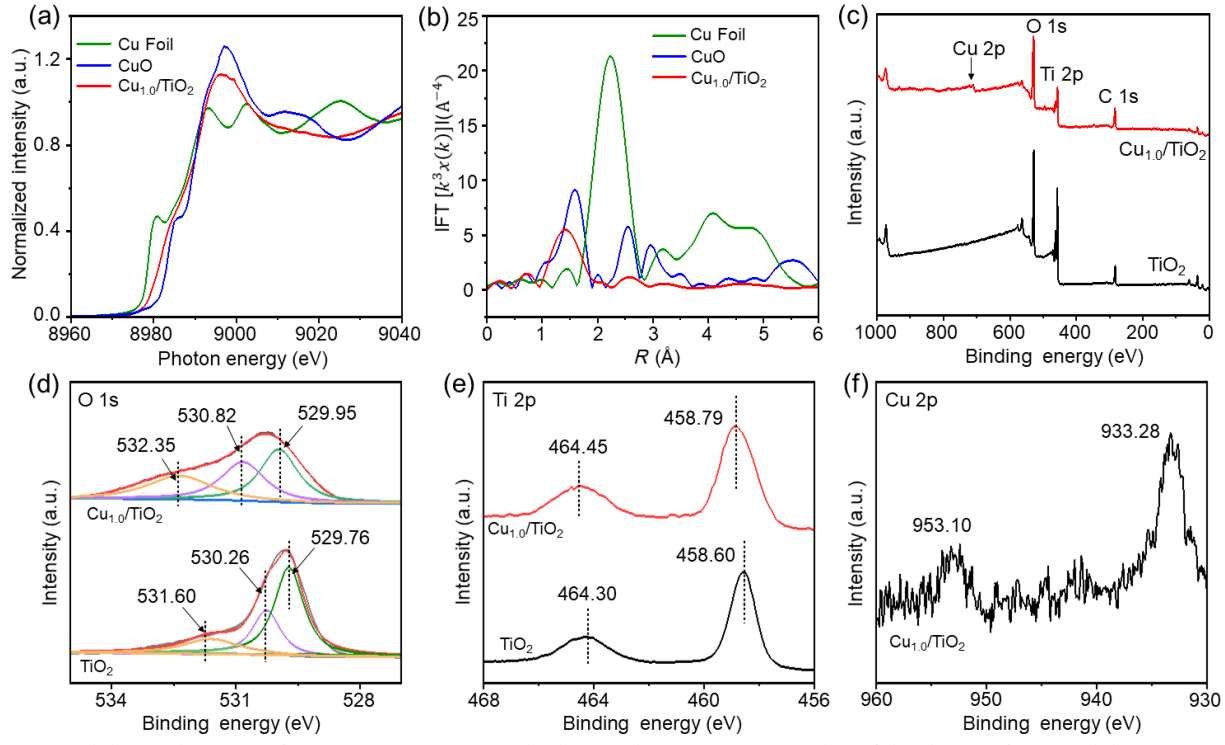


Figure 3 ((a) and (b)) Local structure of $Cu_{1.0}/TiO_2$ ADMs: (a) normalized Cu K-edge XANES spectra with Cu-foil and CuO reference and (b) FT-EXAFS spectra with Cu-foil and CuO reference. ((c)–(f)) Survey spectra and high resolution XPS spectra for both TiO_2 and $Cu_{1.0}/TiO_2$ ADMs. (c) Survey spectra, (d) O 1s, (e) Ti 2p, and (f) Cu 2p.

towards CO_2 reduction was systematically evaluated under visible light irradiation. As shown in Fig. 4(a), the $Cu_{1.0}/TiO_2$ exhibits a dramatically enhanced CO evolution rate compared to pristine TiO_2, achieving a ca. 10-fold increase in yield under ambient conditions at room temperature (25 °C), and no external thermal heating system was applied during the reaction. In contrast, pristine TiO_2 produces only trace amounts of CO and CH_4, highlighting the pivotal role of atomically dispersed Cu species in activating CO_2 molecules and facilitating interfacial charge transfer [44, 45]. Notably, CO is the dominant product for both catalysts, while CH_4 is generated in much smaller quantities, indicating a high selectivity towards the two-electron reduction pathway ($CO_2 + 2H^+ + 2e^- \rightarrow CO + H_2O$). The time-dependent photocatalytic activity of $Cu_{1.0}/TiO_2$ is presented in Fig. 4(b). The CO production increases monotonically with irradiation time, reaching a maximum cumulative yield after 6 h, while CH_4 formation remains relatively low throughout the reaction. The linear increase in CO yield suggests sustained catalytic activity without noticeable deactivation or saturation of active sites during the reaction period. This behavior confirms the efficient separation and continuous utilization of photogenerated charge carriers enabled by the Cu and TiO_2 interface. The effect of Cu loading on photocatalytic efficiency was further investigated (Fig. 4(c)). The catalytic activity follows a volcano-type trend, where $Cu_{1.0}/TiO_2$ shows the highest CO yield of 102.51 μmol·g^{-1} with a maximal CO selectivity of 94%. Lower Cu content (0.5 wt.%) results in insufficient active sites for effective CO_2 adsorption and activation, showing a low CO yield. Furthermore, excessive Cu loading (2.0 wt.%) leads to a decline in both activity and selectivity. This deterioration at higher loadings can be attributed to the aggregation of Cu species into clusters or nanoparticles, which can act as recombination centers for photogenerated carriers rather than catalytic active sites, and alter the reaction pathway to favor competing side reactions (e.g., H_2 evolution). Thus, 1.0 wt.% Cu represents the optimal balance between active site density and charge-transfer efficiency [45].

To assess the durability of the photocatalyst, consecutive cycling experiments were conducted (Fig. 4(d)). The $Cu_{1.0}/TiO_2$ maintains a consistent CO yield over three successive reaction runs, with no observable decay in activity or selectivity. This sustained performance attests to the robust stability of the catalyst, consistent with the SMSI revealed by the XPS and XAFS analyses, which prevents the leaching or agglomeration of atomically dispersed Cu species during photocatalysis. Moreover, the CO yield (102.51 μmol·g^{-1}) and selectivity (94%) of $Cu_{1.0}/TiO_2$ are comparable with the recently reported TiO_2-based photocatalysts (Table S5 in the ESM). To rigorously verify that the generated products originate from the photocatalytic CO_2 reduction rather than organic contaminants or instrument artifacts, a series of control experiments were performed (Fig. 4(e)). No detectable carbon products can be observed in the absence of the photocatalyst, light irradiation, or CO_2 (replaced by Ar), confirming that all three components are indispensable for the reaction. Absence of liquid products is further confirmed by nuclear magnetic resonance (NMR) spectroscopic analysis (Fig. S6 in the ESM). Furthermore, isotopic labeling experiments using $^{13}CO_2$ provided direct evidence of the carbon source (Fig. 3(f)). The mass spectra clearly display a dominant signal at m/z = 29, corresponding to ^{13}CO, alongside the $^{13}CO_2$ signal at m/z = 45. The explicit detection of ^{13}CO, matching the retention time in the gas chromatogram (inset of Fig. 4(f)), unambiguously confirms that the generated CO is derived from the reduction of the CO_2 feedstock [46].

2.3 Photoelectrochemical analysis

To gain comprehensive insights into the separation efficiency of

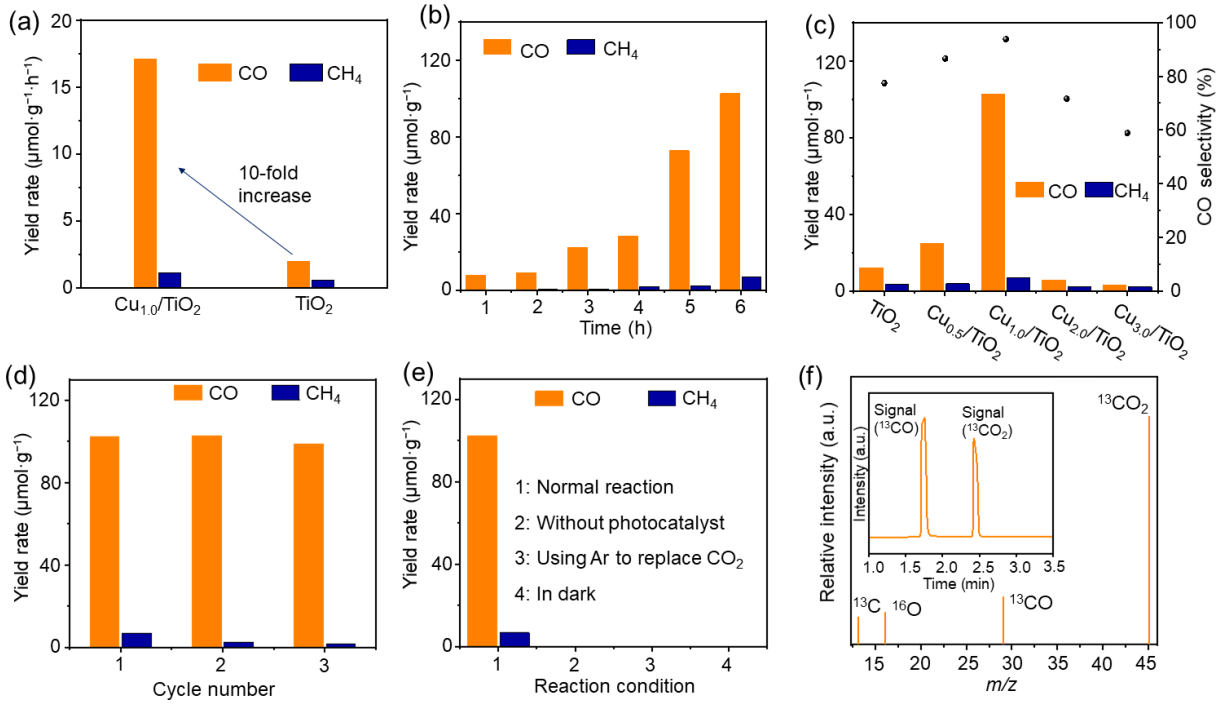


Figure 4 Photocatalytic CO_2 reduction performance of Cu/TiO_2 catalysts. (a) Comparison analysis of pristine TiO_2 and $Cu_{1.0}/TiO_2$ for evolution of CO and CH_4. (b) Time-dependent CO and CH_4 production over $Cu_{1.0}/TiO_2$. (c) Effect of Cu loading on CO_2 reduction activity and CO selectivity. (d) Cyclic stability of $Cu_{1.0}/TiO_2$ over three consecutive reaction runs. (e) Control experiments under different reaction conditions of $Cu_{1.0}/TiO_2$. (f) $^{13}CO_2$ labelling experiment of $Cu_{1.0}/TiO_2$.

photogenerated electron–hole pairs, photoluminescence (PL) spectroscopy was employed (Fig. 5(a)). Upon excitation at 375 nm, pristine TiO_2 exhibits a broad emission peak centered ca. 430–450 nm, which originates from the radiative recombination of photogenerated carriers. In contrast, the PL intensity of the $Cu_{1.0}/TiO_2$ is significantly suppressed [47, 48]. This significant quenching effect indicates that the atomically dispersed Cu sites function as effective electron traps, thereby inhibiting the radiative recombination of electron–hole pairs and promoting interfacial charge transfer. The textural properties of the catalysts were investigated using N_2 adsorption–desorption isotherms (Fig. 5(b)) [41]. The $Cu_{1.0}/TiO_2$ samples display a Type IV isotherm with a distinct hysteresis loop, characteristic of a mesoporous structure. The pore size distribution curve further confirms the presence of mesopores (inset of Fig. 5(b)). This hierarchical porous architecture is highly beneficial for photocatalysis, as it not only provides abundant surface active sites for CO_2 adsorption but also facilitates the mass transport of reactants and products, enhancing the overall reaction kinetics. In addition, specific surface area data are summarized in Table S6 and Fig. S7 in the ESM.

To further verify the separation and migration behavior of photogenerated charge carriers, transient photocurrent responses over the prepared samples were recorded (Fig. 5(c)). Under intermittent light irradiation, both samples show rapid and reversible photocurrent responses. Notably, $Cu_{1.0}/TiO_2$ generates a significantly higher and more stable photocurrent density (ca. 3.1 μA·cm^{-2}) compared to pristine TiO_2 (ca. 2.4 μA·cm^{-2}). This enhancement demonstrates that Cu incorporation effectively improves the photogenerated charge carrier utilization efficiency. In addition, electrochemical impedance spectroscopy (EIS) was performed to analyze the charge transfer resistance (Fig. 5(d)). The Nyquist plots reveal that the arc radius of $Cu_{1.0}/TiO_2$ is substantially smaller than that of pure TiO_2. Since the arc radius is directly proportional to the interfacial charge-transfer resistance (R_{ct}), this result signifies that Cu species dramatically reduce the resistance for electron transfer. Additionally, linear sweep voltammetry (LSV) measurements shown in Fig. S8 in the ESM indicate that $Cu_{1.0}/TiO_2$ exhibits a higher current density than TiO_2 under the same applied potential. Collectively, the suppressed PL intensity, enhanced photocurrent, and reduced charge-transfer resistance provide robust evidence that the $Cu_{1.0}/TiO_2$ possesses superior photogenerated charge separation efficiency and faster surface reaction kinetics, which are the key drivers for the observed enhancement in photocatalytic CO_2 reduction performance [49].

2.4 *In-situ* diffuse reflectance Fourier transform infrared spectroscopy (DRIFTS) and DFT analysis

To strictly delineate the molecular trajectory of the photocatalytic CO_2 reduction and identify the rate-determining intermediates, *in-situ* DRIFTS was employed to monitor the surface reaction dynamics on both pristine TiO_2 and $Cu_{1.0}/TiO_2$. Under the continuous flow of CO_2 and visible light irradiation, the $Cu_{1.0}/TiO_2$ exhibits a rich and evolving landscape of surface species (Fig. 6(a)), offering a stark contrast to the chemically inert surface of pristine TiO_2 (Fig. 6(b)). Detailed spectral analysis of the $Cu_{1.0}/TiO_2$ reveals the emergence of several critical vibrational bands that intensify monotonically with irradiation time. Most notably, the distinct absorption band centered at approximately 1680 cm^{-1} is assigned to the carboxyl radical (COOH*). The detection of this species is of paramount importance, as the protonation of adsorbed CO_2 to form COOH* ($CO_2 + H^+ + e^- \rightarrow$ COOH*) is widely regarded as the rate-determining step in the conversion of CO_2 to CO. Additionally, the spectra display a band at 1630 cm^{-1}, corresponding to adsorbed water or surface hydroxyls, which serve as the essential proton source for the reduction process. The appearance of band near 1590 cm^{-1} corresponds to formyl intermediate (CHO*). Other

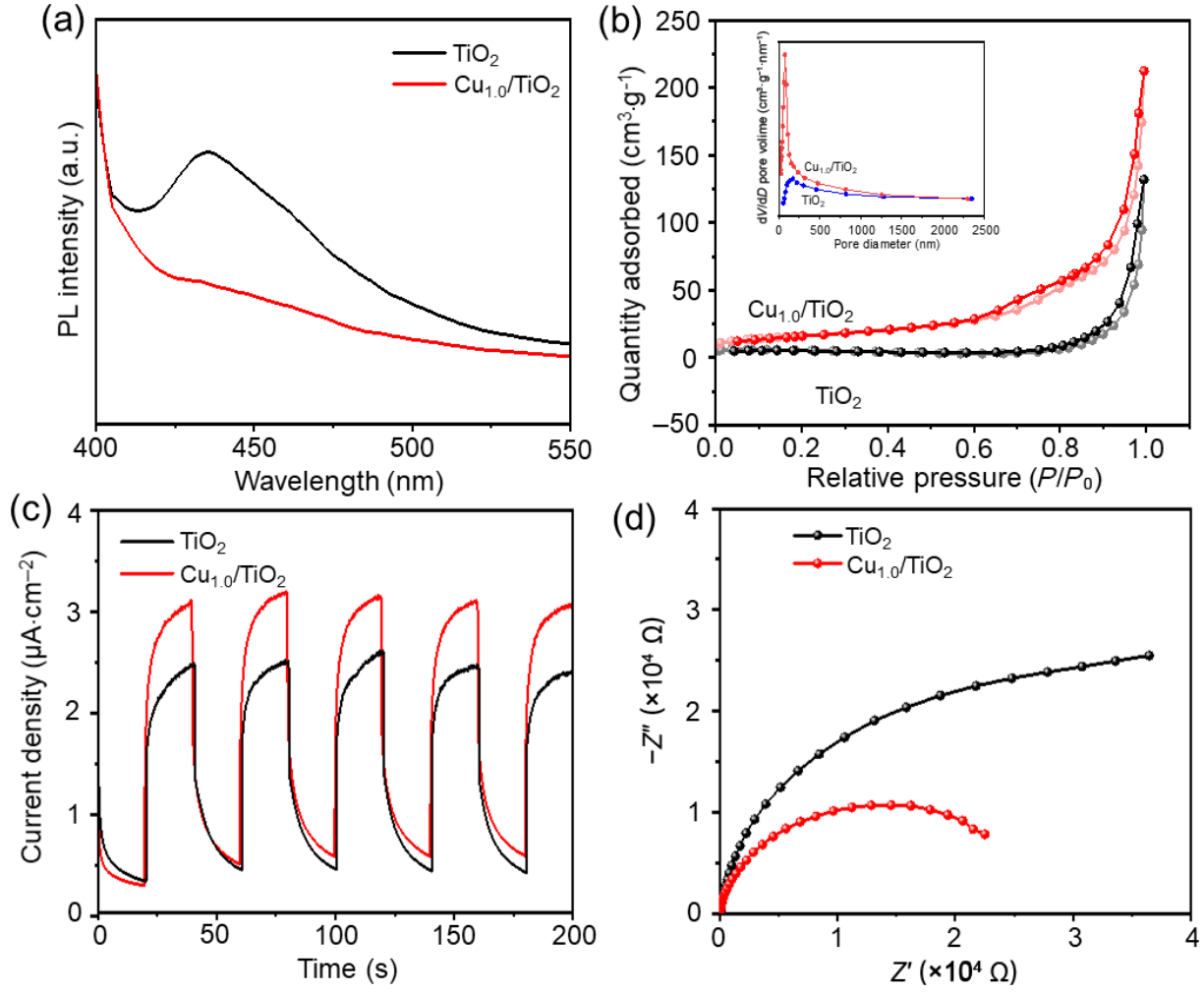


Figure 5 (a) PL emission spectra of TiO_2 and $Cu_{1.0}/TiO_2$. (b) N_2 adsorption–desorption isotherms of TiO_2 and $Cu_{1.0}/TiO_2$ (inset: the pore size distribution of TiO_2 and $Cu_{1.0}/TiO_2$). (c) Transient photocurrent response of TiO_2 and $Cu_{1.0}/TiO_2$ under intermittent light irradiation. (d) EIS Nyquist plot of TiO_2 and $Cu_{1.0}/TiO_2$.

prominent peaks in the 1530–1580 and 1300–1480 cm^{-1} regions are attributed to bicarbonate (HCO_3^-) and various carbonate species (such as m-CO_3^{2-} and b-CO_3^{2-}), respectively, indicating that the basic surface hydroxyl groups actively facilitate the initial capture of CO_2 molecules [43]. Conversely, the spectra for pristine TiO_2 display negligible signal evolution under identical conditions. The absence of the characteristic COOH* peak on TiO_2 suggests a high activation energy barrier for the initial hydrogenation step, resulting in its poor photocatalytic activity.

The dramatic enhancement in signal intensity and the clear time-dependent accumulation of intermediates on $Cu_{1.0}/TiO_2$ confirm that the atomically dispersed Cu sites act as highly efficient electron collectors [50, 51]. These sites not only stabilize the thermodynamically unstable COOH* intermediate but also effectively lower the activation barrier for the C–O bond cleavage. Consequently, the spectroscopic evidence strongly supports an associative reaction pathway where the Cu–TiO_2 interface drives the selective reduction of CO_2 through a stable carboxyl intermediate, preventing the desorption of unreacted species and suppressing competing side reactions [52]. The optimised geometries (Figs. 6(c)–6(f)) reveal that CO_2 adsorbs weakly on pristine TiO_2, whereas the presence of Cu significantly enhances CO_2 interaction with the surface. The corresponding charge density difference models show pronounced electron accumulation around the adsorbed CO_2 and the charge depletion near the Cu–TiO_2 interface, indicating effective charge transfer from the catalyst to CO_2. This electron redistribution highlights the role of Cu anchoring in promoting CO_2 activation.

3 Conclusions

In summary, a facile and scalable Joule heating strategy was successfully established to fabricate robust and atomically dispersed Cu species on TiO_2. The ultrafast thermal shock process effectively suppresses metal aggregation and ensures the formation of strongly anchored Cu atomically dispersed metal species via enhanced metal–support interactions. The optimized $Cu_{1.0}/TiO_2$ exhibits markedly enhanced photocatalytic CO_2 reduction performance, achieving high CO yield and selectivity. Comprehensive experimental and spectroscopic investigations reveal that this superior activity originates from a synergistic mechanism, where the incorporation of Cu not only modulates the band structure to increase the thermodynamic driving force but also serves as an efficient electron trap to suppress charge recombination and accelerate interfacial charge transfer. Crucially, *in-situ* DRIFTS analysis provides molecular-level evidence that these atomically dispersed Cu sites effectively stabilize the key COOH* intermediate, thereby significantly lowering the activation energy barrier for CO

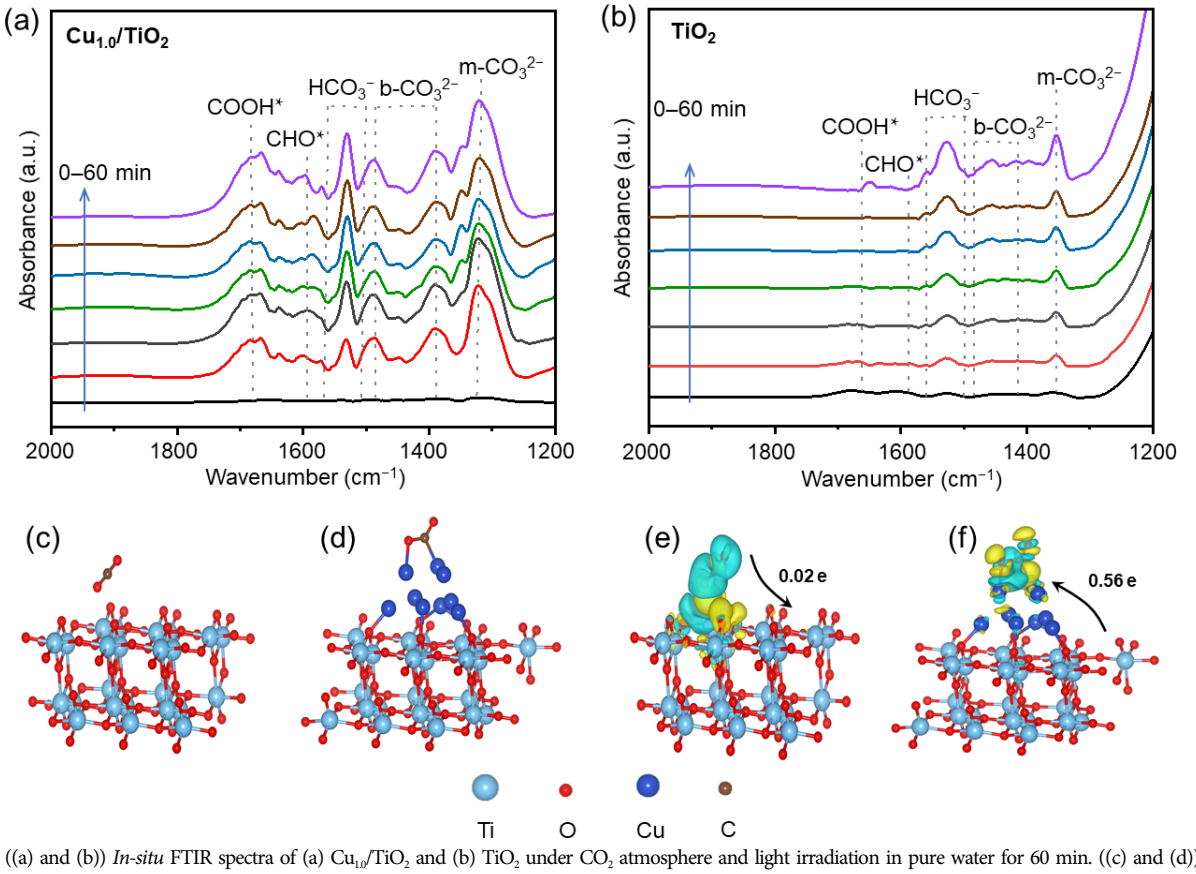


Figure 6 ((a) and (b)) *In-situ* FTIR spectra of (a) $Cu_{1.0}/TiO_2$ and (b) TiO_2 under CO_2 atmosphere and light irradiation in pure water for 60 min. ((c) and (d)) Three-dimensional (3D) models of the Optimized (c) TiO_2 and (d) $Cu_{1.0}/TiO_2$ adsorbed with CO_2. ((e) and (f)) 3D models of the charge density difference of (e) TiO_2 and (f) $Cu_{1.0}/TiO_2$ adsorbed with CO_2 with an isosurface of 1.5×10^{-3} e·Å^{-3} (the charge accumulation is shown as the yellow region, and the charge depletion is shown as the cyan region).

evolution. Overall, this work demonstrates an atomic-level photocatalyst design enabled by a rapid and energy-efficient synthesis route. It highlights the universality of Joule heating for preparing stable atomically dispersed metal atom catalysts and provides a promising platform for the development of advanced materials for sustainable solar-to-chemical energy conversion applications.

Electronic Supplementary Material: Supplementary material (experimental section, DFT studies catalyst characterization images, and test results) is available in the online version of this article at https://doi.org/10.26599/NR.2026.94908854.

Data availability

All data needed to support the conclusions in the paper are presented in the manuscript and the Electronic Supplementary Material. Additional data related to this paper may be requested from the corresponding author upon request.

Acknowledgement

This work was supported by the National Key Research and Development Program of China (Nos. 2020YFA0710302 and 2022YFE0126500), the National Natural Science Foundation of China (Nos. 52261135635, 22150610467, and 22232003), and the Anhui Provincial Natural Science Foundation (No. 2408085MB024).

Declaration of competing interest

All the contributing authors report no conflict of interests in this work.

Author contribution statement

K. T. K: Data curation, project administration, validation, writing manuscript, experimental design. J. L: Data curation, project administration, validation, writing manuscript, experimental design. Z. L. W: Project administration, funding acquisition, writing manuscript. S. K. S.: Data curation, project administration, validation, writing manuscript, experimental design. Y. L.: Data curation, project administration, validation, writing manuscript, experimental design. S. M.: Data curation, project administration, validation, writing manuscript, experimental design. Z. I.: Data curation, project administration, validation, writing manuscript, experimental design. C. Z.: Project administration, funding acqisition, writing manuscript. J. X. L.: Project administration, funding acquisition, writing manuscript. R. L.: Project administration, funding acquisition, writing manuscript. Y. J. X.: Project administration, funding acquisition, writing manuscript. All the authors have approved the final manuscript.

Use of AI statement

None.

References

[1] Yao, S.; He, J. Q.; Gao, F.; Wang, H. W.; Lin, J. H.; Bai, Y.; Fang, J. Y.; Zhu, F.; Huang, F.; Wang, M. Y. Highly selective semiconductor photocatalysis for CO_2 reduction. *J. Mater. Chem. A* **2023**, *11*, 12539–12558.

[2] Wang, Y. O.; Chen, E. Q.; Tang, J. W. Insight on reaction pathways of photocatalytic CO_2 conversion. *ACS Catal.* **2022**, *12*, 7300–7316.

[3] Rawool, S. A.; Yadav, K. K.; Polshettiwar, V. Defective TiO_2 for photocatalytic CO_2 conversion to fuels and chemicals. *Chem. Sci.* **2021**, *12*, 4267–4299.

[4] Liao, L.; Xie, G. S.; Xie, X. Q.; Zhang, N. Advances in modulating the activity and selectivity of photocatalytic CO_2 reduction to multicarbon products. *J. Phys. Chem. C* **2023**, *127*, 2766–2781.

[5] Jiang, W. B.; Low, J.; Mao, K. K.; Duan, D. L.; Chen, S. M.; Liu, W.; Pao, C. W.; Ma, J.; Sang, S. K.; Shu, C. et al. Pd-modified ZnO-Au enabling alkoxy intermediates formation and dehydrogenation for photocatalytic conversion of methane to ethylene. *J. Am. Chem. Soc.* **2021**, *143*, 269–278.

[6] Hu, W. Y.; Yang, H. Y.; Wang, C. Y. Progress in photocatalytic CO_2 reduction based on single-atom catalysts. *RSC Adv.* **2023**, *13*, 20889–20908.

[7] Syal, B.; Kumar, P.; Gupta, P. Recent advancements in the preparation and application of copper single-atom catalysts. *ACS Appl. Nano Mater.* **2023**, *6*, 4987–5041.

[8] Chen, J. Q.; Li, T. X.; An, X. F.; Fu, D. Photocatalytic reduction of CO_2 by TiO_2 modified materials: Recent advances and outlook. *Energy Fuels* **2024**, *38*, 7614–7636.

[9] Hossen, M. A.; Solayman, H. M.; Leong, K. H.; Sim, L. C.; Yaacof, N.; Aziz, A. A.; Wu, L. H.; Monir, M. U. Recent progress in TiO_2-based photocatalysts for conversion of CO_2 to hydrocarbon fuels: A systematic review. *Results Eng.* **2022**, *16*, 100795.

[10] Tasbihi, M.; Kočí, K.; Troppová, I.; Edelmannová, M.; Reli, M.; Čapek, L.; Schomäcker, R. Photocatalytic reduction of carbon dioxide over Cu/TiO_2 photocatalysts. *Environ. Sci. Pollut. Res.* **2018**, *25*, 34903–34911.

[11] Huang, G. F.; Shen, Q. Y.; Ma, X. Y.; Zhong, J. B.; Chen, J. F.; Huang, J. W.; Wang, L.; She, H. D.; Wang, Q. Z. Preparation of an In_2S_3/TiO_2 heterostructure for enhanced activity in carbon dioxide photocatalytic reduction. *ChemPhotoChem* **2021**, *5*, 438–444.

[12] Zhang, J.; Zheng, C. Y.; Zhang, M. L.; Qiu, Y. J.; Xu, Q.; Cheong, W. C.; Chen, W. X.; Zheng, L. R.; Gu, L.; Hu, Z. P. et al. Controlling N-doping type in carbon to boost single-atom site Cu catalyzed transfer hydrogenation of quinoline. *Nano Res.* **2020**, *13*, 3082–3087.

[13] Gao, C.; Chen, S. M.; Wang, Y.; Wang, J. W.; Zheng, X. S.; Zhu, J. F.; Song, L.; Zhang, W. K.; Xiong, Y. J. Heterogeneous single-atom catalyst for visible-light-driven high-turnover CO_2 reduction: The role of electron transfer. *Adv. Mater.* **2018**, *30*, 1704624.

[14] Wang, X. Q.; Chen, Z.; Zhao, X. Y.; Yao, T.; Chen, W. X.; You, R.; Zhao, C. M.; Wu, G.; Wang, J.; Huang, W. X. et al. Regulation of coordination number over single Co sites: Triggering the efficient electroreduction of CO_2. *Angew. Chem., Int. Ed.* **2018**, *57*, 1944–1948.

[15] Yang, H. Z.; Shang, L.; Zhang, Q. H.; Shi, R.; Waterhouse, G. I. N.; Gu, L.; Zhang, T. R. A universal ligand mediated method for large scale synthesis of transition metal single atom catalysts. *Nat. Commun.* **2019**, *10*, 4585.

[16] Rehman, Z. U.; Bilal, M.; Hou, J. H.; Butt, F. K.; Ahmad, J.; Ali, S.; Hussain, A. Photocatalytic CO_2 reduction using TiO_2-based photocatalysts and TiO_2 Z-scheme heterojunction composites: A review. *Molecules* **2022**, *27*, 2069.

[17] Alencar, C. S. L.; Paiva, A. R. N.; Silva, J. C. M. D.; Vaz, J. M.; Spinacé, E. V. One-step synthesis of $AuCu/TiO_2$ catalysts for CO preferential oxidation. *Mater. Res.* **2020**, *23*, e20200181.

[18] Raguram, T.; Rajni, K. S. Synthesis and analysing the structural, optical, morphological, photocatalytic and magnetic properties of TiO_2 and doped (Ni and Cu) TiO_2 nanoparticles by sol-gel technique. *Appl. Phys. A* **2019**, *125*, 288.

[19] Zhang, W. Q.; Fu, C. F.; Low, J.; Duan, D. L.; Ma, J.; Jiang, W. B.; Chen, Y. H.; Liu, H. J.; Qi, Z. M.; Long, R. et al. High-performance photocatalytic nonoxidative conversion of methane to ethane and hydrogen by heteroatoms-engineered TiO_2. *Nat. Commun.* **2022**, *13*, 2806.

[20] Gao, C.; Low, J.; Long, R.; Kong, T. T.; Zhu, J. F.; Xiong, Y. J. Heterogeneous single-atom photocatalysts: Fundamentals and applications. *Chem. Rev.* **2020**, *120*, 12175–12216.

[21] Zhang, Y. Q.; Xu, N.; Liu, Y.; Zhang, X. S.; Li, W. Z.; Zhao, H. T.; Luan, J. Synthesis of a 2D $Cu@TiO_2$ composite via the design of a 1D Cu-based coordination polymer precursor for efficient and selective photodegradation of dyes. *RSC Adv.* **2022**, *12*, 9363–9372.

[22] He, G. C.; Yan, M. M.; Gong, H. S.; Fei, H. L.; Wang, S. Y. Ultrafast synthetic strategies under extreme heating conditions toward single-atom catalysts. *Int. J. Extrem. Manuf.* **2022**, *4*, 032003.

[23] Xiong, Q.; Zhu, X. B.; He, R.; Mei, X. Y.; Zhang, Y. X.; Zhong, Z. C.; Zhao, W.; Nie, W. M.; Zhang, J. Local Joule heating targets catalyst surface for hydrocarbon combustion. *J. Ind. Eng. Chem.* **2023**, *117*, 273–281.

[24] Li, J. Q.; Luo, L. Y.; Wang, S. Y.; Song, H. J.; Jiang, B. J. Recent advances in Joule-heating synthesis of functional nanomaterials for photo and electrocatalysis. *PhotoMat*, in press, DOI: 10.1002/phmt.14.

[25] Zhang, Y. M.; Zhao, J. H.; Wang, H.; Xiao, B.; Zhang, W.; Zhao, X. B.; Lv, T. P.; Thangamuthu, M.; Zhang, J.; Guo, Y. et al. Single-atom Cu anchored catalysts for photocatalytic renewable H_2 production with a quantum efficiency of 56%. *Nat. Commun.* **2022**, *13*, 58.

[26] Li, M. C.; Qin, N.; Ji, Z. W.; Gan, Q. M.; Wang, Z. Y.; Li, Y. Z.; Cao, L. J.; Yuan, H. M.; He, D. S.; Chen, Z. H. et al. Single copper sites dispersed on defective TiO_{2-x} as a synergistic oxygen reduction reaction catalyst. *J. Chem. Phys.* **2021**, *154*, 034705.

[27] Xi, D. W.; Li, J. Y.; Low, J.; Mao, K. K.; Long, R.; Li, J. W.; Dai, Z. H.; Shao, T. Y.; Zhong, Y.; Li, Y. et al. Limiting the uncoordinated N species in $M\text{-}N_x$ single-atom catalysts toward electrocatalytic CO_2 reduction in broad voltage range. *Adv. Mater.* **2022**, *34*, 2104090.

[28] Wyss, K. M.; Luong, D. X.; Tour, J. M. Large-scale syntheses of 2D materials: Flash joule heating and other methods. *Adv. Mater.* **2022**, *34*, 2106970.

[29] Wulan, B. R.; Cao, X. Y.; Tan, D. X.; Ma, J. Z.; Zhang, J. T. To stabilize oxygen on In/In_2O_3 heterostructure via joule heating for efficient electrocatalytic CO_2 reduction. *Adv. Funct. Mater.* **2023**, *33*, 2209114.

[30] Noh, S. H.; Eom, W.; Lee, W. J.; Park, H.; Ambade, S. B.; Kim, S. O.; Han, T. H. Joule heating-induced sp^2-restoration in graphene fibers. *Carbon* **2019**, *142*, 230–237.

[31] Yao, Y. G.; Huang, Z. N.; Xie, P. F.; Wu, L. P.; Ma, L.; Li, T. Y.; Pang, Z. Q.; Jiao, M. L.; Liang, Z. Q.; Gao, J. L. et al. High temperature shockwave stabilized single atoms. *Nat. Nanotechnol.* **2019**, *14*, 851–857.

[32] Wei, S. J.; Li, A.; Liu, J. C.; Li, Z.; Chen, W. X.; Gong, Y.; Zhang, Q. H.; Cheong, W. C.; Wang, Y.; Zheng, L. R. et al. Direct observation of noble metal nanoparticles transforming to thermally stable single atoms. *Nat. Nanotechnol.* **2018**, *13*, 856–861.

[33] Zhu, X. D.; Wen, G. L.; Liu, H.; Han, S. H.; Chen, S. H.; Kong, Q. Q.; Feng, W. One-step hydrothermal synthesis and characterization of Cu-doped TiO_2 nanoparticles/nanobucks/nanorods with enhanced photocatalytic performance under simulated solar light. *J. Mater. Sci. Mater. Electron.* **2019**, *30*, 13826–13834.

[34] Choudhury, B.; Dey, M.; Choudhury, A. Defect generation, d–d transition, and band gap reduction in Cu-doped TiO_2 nanoparticles. *Int. Nano Lett.* **2013**, *3*, 25.

[35] Katherine, T. N. L.; Vendula, B.; Jaroslav, K.; Jaroslav, C. Structure

and Photocatalytic properties of Ni-, Co-, Cu-, and Fe-doped TiO_2 aerogels. *Gels* **2023**, *9*, 357.

[36] Wang, W. S.; Wei, D. L.; Zhang, Y.; Ye, Y. F.; Dou, Y.; Guo, J. H.; Yan, M.; Yin, Y. D. Photoreversible color-switching Cu-doped TiO_2 nanoparticles for high-contrast rewritable printing. *ACS Nano* **2024**, *18*, 34186–34194.

[37] Bhattacharyya, K.; Mane, G. P.; Rane, V.; Tripathi, A. K.; Tyagi, A. K. Selective CO_2 photoreduction with Cu-doped TiO_2 photocatalyst: Delineating the crucial role of Cu-oxidation state and oxygen vacancies. *J. Phys. Chem. C* **2021**, *125*, 1793–1810.

[38] Ansari, S. A.; Cho, M. H. Highly visible light responsive, narrow band gap TiO_2 nanoparticles modified by elemental red phosphorus for photocatalysis and photoelectrochemical applications. *Sci. Rep.* **2016**, *6*, 25405.

[39] Wang, T.; Sun, F. L.; Liu, S. J.; Zhuang, G. L.; Li, B. X. Dioxygen-enhanced CO_2 photoreduction on TiO_2 supported Cu single-atom sites. *Appl. Catal. B: Environ.* **2023**, *325*, 122339.

[40] Li, H. M.; He, W. X.; Xu, L. X.; Pan, Y.; Xu, R. C.; Sun, Z. H.; Wei, S. Q. Synergistic interface between metal Cu nanoparticles and CoO for highly efficient hydrogen production from ammonia borane. *RSC Adv.* **2023**, *13*, 11569–11576.

[41] Yin, H. B.; Dong, F.; Wang, D. S.; Li, J. H. Coupling Cu single atoms and phase junction for photocatalytic CO_2 reduction with 100% CO selectivity. *ACS Catal.* **2022**, *12*, 14096–14105.

[42] Qian, F. R.; Cao, D. F.; Chen, S. M.; Yuan, Y. L.; Chen, K.; Chimtali, P. J.; Liu, H. J.; Jiang, W.; Sheng, B. B.; Yi, L. C. et al. High-entropy RuO_2 catalyst with dual-site oxide path for durable acidic oxygen evolution reaction. *Nat. Commun.* **2025**, *16*, 6894.

[43] Shen, Y.; Ren, C. J.; Zheng, L. R.; Xu, X. Y.; Long, R.; Zhang, W. Q.; Yang, Y.; Zhang, Y. C.; Yao, Y. F.; Chi, H. Q. et al. Room-temperature photosynthesis of propane from CO_2 with Cu single atoms on vacancy-rich TiO_2. *Nat. Commun.* **2023**, *14*, 1117.

[44] Jiao, X. C.; Zheng, K.; Liang, L.; Li, X. D.; Sun, Y. F.; Xie, Y. Fundamentals and challenges of ultrathin 2D photocatalysts in boosting CO_2 photoreduction. *Chem. Soc. Rev.* **2020**, *49*, 6592–6604.

[45] Bi, W. T.; Wu, C. Z.; Xie, Y. Atomically thin two-dimensional solids: An emerging platform for CO_2 electroreduction. *ACS Energy Lett.* **2018**, *3*, 624–633.

[46] Chen, P. J.; Li, Z. J.; Wang, P. Z.; Yao, Y. X.; Dou, T. W.; Qu, Y.; Jing, L. Q. Synergistic effect of atomically dispersed Cu species and Ti-defects for boosting photocatalytic CO_2 reduction over hierarchical TiO_2. *Nanoscale* **2024**, *16*, 10727–10736.

[47] Lim, S. P.; Pandikumar, A.; Lim, H. N.; Ramaraj, R.; Huang, N. M. Boosting photovoltaic performance of dye-sensitized solar cells using silver nanoparticle-decorated N,S-co-doped-TiO_2 photoanode. *Sci. Rep.* **2015**, *5*, 11922.

[48] Tang, M.; Yang, D. X.; Wang, J.; Zhou, Q.; Zhu, X. D.; Jiao, Y. Effects of Cu doping on the phase transition and photocatalytic activity of anatase/rutile mixed crystal TiO_2 nanocomposites. *Mater. Res. Express* **2021**, *8*, 085007.

[49] Li, D.; Zhao, Y. X.; Zhou, C.; Zhang, L. P.; Tang, J. W.; Zhang, T. R. Unveiling the critical role of TiO_2-supported atomically dispersed Cu species for enhanced photofixation of N_2 to nitrate. *Fund. Res.* **2024**, *4*, 934–940.

[50] Liu, P. G.; Huang, Z. X.; Gao, X. P.; Hong, X.; Zhu, J. F.; Wang, G. M.; Wu, Y. E.; Zeng, J.; Zheng, X. S. Synergy between palladium single atoms and nanoparticles via hydrogen spillover for enhancing CO_2 photoreduction to CH_4. *Adv. Mater.* **2022**, *34*, 2200057.

[51] Ning, C. J.; Yang, J. R.; Bai, S.; Chen, G. B.; Liu, G. H.; Shen, T. Y.; Zheng, L. R.; Xu, S. M.; Kong, X. G.; Liu, B. et al. An efficient intercalation supramolecular structure for photocatalytic CO_2 reduction to ethylene under visible light. *Adv. Funct. Mater.* **2023**, *33*, 2300365.

[52] Zhou, G. L.; Yang, J. M.; Zhu, X. W.; Li, Q. D.; Yu, Q.; El-Alami, W.; Wang, C. T.; She, Y. B.; Qian, J. C.; Xu, H. et al. Cryo-induced closely bonded heterostructure for effective CO_2 conversion: The case of ultrathin BP nanosheets/g-C_3N_4. *J. Energy Chem.* **2020**, *49*, 89–95.

This is an open access article under the terms of the Creative Commons Attribution 4.0 International License (CC BY 4.0, https://creativecommons.org/licenses/by/4.0/).

© The Author(s) 2026. Published by Tsinghua University Press.